Kaihe Yamazaki[1,2,3], Shigeru Aoki[1], Kohei Mizobata[4]

[1] Institute of Low Temperature Science, Hokkaido University, Hokkaido, Japan

[2] Graduate School of Environmental Science, Hokkaido University, Hokkaido, Japan

[3] National Institute of Polar Research, Tokyo, Japan

[4] Tokyo University of Marine Science and Technology, Tokyo, Japan

Corresponding author: Kaihe Yamazaki (kaiheyamazaki@gmail.com)

Key Points

- Eddy diffusivity in the subpolar Southern Ocean is estimated to be 100–500 m^2 s^{-1} based on hydrographic variability and satellite altimetry.
- Eddy heat flux towards the Wilkes Land is ~3.6 TW, nearly balancing with surface freezing, glacial melt, and solar heating.
- The thickness gradient controls mixing length and eddy diffusivity in the subpolar zone.

Abstract

Warm, salty Circumpolar Deep Water (CDW) is recognized as the primary driver for Antarctic glacial melt, but the mechanism by which it reaches the continental shelves remains highly uncertain from an observational standpoint. With the scarcity of eddy flux estimation in the Antarctic margin, we quantify the isopycnal diffusivity of CDW using hydrographic variability and satellite altimetry under the mixing length framework. For comparison, the spiciness and thickness are used as isopycnal tracers, and the two tracers yield qualitatively similar estimates. Over the Antarctic Circumpolar Current (ACC), spatial variation of mixing length is generally aligned with the jet-induced mixing suppression theory, including its exception in the lee of the topography. In contrast, the mixing length does not depend on the mean flow in the subpolar zone, likely reflecting the relatively quiescent flow regime. The estimated isopycnal diffusivity ranges from 100 to 500 m^2 s^{-1} south of the ACC. The eddy diffusivity tends to be enhanced where the gradient of isopycnal thickness becomes small and CDW intrudes onshore. The cross-slope eddy CDW flux is estimated, and the associated onshore heat flux across is calculated as ~3.6 TW in the eastern Indian sector. The eddy heat flux and coastal solar heating are generally balanced with cryospheric heat sinks including glacial melting and surface freezing, suggesting that the eddy advection is substantial for the onshore CDW flux. The thickness field is essential for determining mixing length and eddy fluxes in the subpolar zone, whereas the situation does not hold for the ACC domain.

Plain Language Summary

Deep ocean is a significant source of heat and salt for the Antarctic coasts. Thus, its behavior is relevant for a wide range of climate sciences, such as

Antarctic glacial melt, sea ice variability, and global ocean overturning. The warm deep water is presumably transported to the Antarctic coasts by ocean eddies, but observational evidence has not been provided to date. By synthesizing ocean measurements and satellite altimetry, we estimate the eddy-driven onshore transport of the deep water over the Antarctic margin. It is shown that shoreward heat transport by eddies is generally balanced with heat gain by solar heating and heat loss expected from surface freezing and glacial melt. This result indicates that eddy transport plays a fundamental role in the coastal heat supply. The thickness of the deep water primarily controls the ability to mix along density surfaces that bridge the open ocean to the continental shelves; more homogeneous thickness allows for easier mixing. Our results facilitate the possibility of predicting the diffusion rate of eddies using the thickness of the deep water. This idea is helpful in simulating deep-water transport in global climate models, where sub-grid and unresolved effects of eddies need to be prescribed.

1 Introduction

Throughout the Antarctic Circumpolar Current (ACC), mesoscale eddies transport water masses across time-mean streamlines, comprising the adiabatic pathway of the global meridional overturning circulation (Marshall and Radko, 2003; Cessi, 2019). Isopycnal eddy diffusion is fundamental for the poleward heat flux across the ACC because bottom-enhanced diapycnal mixing (Kunze et al., 2006) and surface water transformation (Abernathey et al., 2016) are unlikely to penetrate the intermediate and deep layers. Recent observations have indicated that mesoscale eddies play a key role in bridging the Antarctic meridional overturning from deep ocean basins to continental shelves (e.g., Mckee et al., 2019; Yamazaki et al., 2021), but its conditioning from the ACC to the Antarctic Slope Current (ASC) largely remains unknown from an observational standpoint (Thompson et al., 2018).

Circumpolar Deep Water (CDW), the primary source of heat and salt for the Antarctic coasts, is transported across the ASC predominantly by mesoscale eddies in the absence of large-scale zonal pressure gradients (Stewart and Thompson, 2013). In reality, the pressure gradient associated with topographic features generates standing eddies and meanders, facilitating meridional water exchange (e.g., Hogg and Blundell, 2006). Topography-controlled geostrophic flows can transport CDW poleward in the continental margin (Morrison et al., 2020; Hirano et al., 2021). However, the steep barotropic potential vorticity (PV) gradient in the upper continental slope (shallower than ~3,000 m isobaths) is unlikely to allow the presence of cross-slope mean flow, and thus eddy diffusion and tidal mixing might be essential to determine the onshore CDW flux near the shelf break (Stewart et al., 2018; Yamazaki et al., 2020). To the south of the ACC, the spatial variability of eddy diffusion has yet to be reported except for Foppert et al. (2019; FRE19), and its controlling factor remains unclear. This study aims to: (1) provide an observational estimate of isopycnal diffusion in the Antarctic margin, which is portrayed as a poleward extension of the estimation by Naveira

Garabato et al. (2011; GFP11), and (2) quantify the isopycnal CDW flux by eddy diffusion towards the continental shelves.

The horizontal circulation in the Antarctic margin is shaped by the subpolar gyres between the ACC and ASC (e.g., Park and Gamberoni, 1995). The Weddell and Ross gyres are wide enough to isolate cold shelf water from warm CDW; in contrast, the proximity of the ACC to the continent creates an eastward slope current in the eastern Pacific sector (Spence et al., 2017; Thompson et al., 2020) and standing eddies in the Indian sector (Mizobata et al., 2020; Yamazaki et al., 2020), resulting in a relatively warmer coastal condition than in the other sectors (e.g., Stokes et al., 2022). The present study targets the Indian sector corresponding to the East Antarctic margin (30–160°E; Fig. 1), where a sufficient amount of in-situ data exists for the estimation. In this region, the eddy conditions have recently been explored (FRE19; Stewart et al., 2018), wherein lateral tidal mixing is known to be weaker than that in the rest of the Antarctic margin (Padman et al., 2018), and the frontal structure of the ASC is relatively prominent (Pauthenet et al., 2021). The onshore CDW flux towards East Antarctica is collecting attention as a cause of glacial melting (e.g., van Wijk et al., 2022).

The remainder of this paper is set out as follows: Section 2 reviews the theoretical background for observation-based eddy diffusivity calculations and introduces the concept of the mixing length framework. Section 3 describes data and methods used for the diffusivity calculations, and Section 4 presents the quantification of the mixing length, eddy diffusivity, and eddy fluxes together with their spatial variations. Lastly, Section 5 assesses the validity of the presented results and discusses controlling factors for eddy diffusion. Section 6 is the conclusion.

2 Theoretical background

The mixing length framework serves as the basis for the analysis. Conventional ways to estimate oceanic eddy diffusion are hydrographic variability (Armi and Stommel, 1983; GFP11) and altimetric eddy scaling (Klocker and Abernathey, 2014; Bates et al., 2014). In both methods, the diffusivity k is obtained via the mixing length formulation (Taylor, 1921):

$$k \;=\; \Gamma U_{\mathrm{eddy}} L_{\mathrm{mix}} \qquad (1),$$

where Γ is mixing efficiency, U_{eddy} is characteristic eddy velocity measured by the standard deviation of downgradient velocity $\sigma(v)$, and L_{mix} is mixing length scale. This formulation relies on two major assumptions: (i) tracer fluctuations are generated by the local stirring of the large-scale tracer gradient, with weak advection of tracer variance from upstream regions; and (ii) the tracer gradient varies slowly over the distance L_{mix}. The validity of these assumptions is confirmed *a posteriori*.

The mixing length framework has been widely applied in the closure of geostrophic turbulence because it can link the eddy tracer transport to the downgradient flux in Eulerian form. Diffusivity k of generalized tracer φ (which approximately follows PV contours) due to isopycnal stirring is parameterized as

$$\overline{v'\varphi'} \;=\; -k\frac{\partial \varphi}{\partial y} \qquad (2),$$

where the overbars indicate the temporal average in the isopycnal layer, the primes indicate deviations from the averages, and the tracer gradient is assumed to be meridional. v is meridional velocity, so the tracer flux is the covariance between tracer anomaly and cross-frontal velocity. Here, it is also assumed that the tracer φ mixes purely along the isopycnal. This assumption is aligned with the conditions where the mixing process is statistically stable, adiabatic, and solely caused by linear waves (e.g., Vallis, 2017). We may choose any tracer for φ if the tracer concentration represents the PV field to the extent of interest, where its diffusion satisfies a requirement for the GM flux mimicking baroclinic instability (Gent and McWilliams, 1990). Then, the scalar coefficient of downgradient flux can express the skew component of the diffusivity tensor. In this framework, GFP11 and FRE19 derived the eddy diffusivity using hydrographic variability of the isopycnal temperature and spiciness (as φ) and inferred the volume transport as a result of the thickness diffusion.

One possible choice for L_{mix} is the characteristic eddy scale determined by an altimetric velocity field (Klocker and Abernathey, 2014; Bates et al., 2014); this approach requires the eddy's deformation radius to be resolved by altimetry. Another choice is an empirical method using hydrographic data. Emulating the arguments of Armi and Stommel (1983), GFP11 estimated L_{mix} in the Southern Ocean from hydrographic variability as follows:

$$L_{\mathrm{mix}} = \frac{\sigma(\varphi)}{|\nabla \varphi|} \qquad (3)$$

Although GFP11 used potential temperature for the isopycnal tracer φ, other tracer variables (e.g., isopycnal spiciness and layer thickness) are possible. From equations (1)–(3), the mixing efficiency is calculated as:

$$\Gamma = \frac{\overline{v'\varphi'}}{\sigma(v)\ \sigma(\varphi)} \qquad (4)$$

This expression is identical to the correlation coefficient between v and φ, but a wide range of estimates exists for Γ (ranging 0.01–0.4; Holloway and Kristmannsson, 1984; Visbeck et al., 1997; Karsten and Marshall, 2002) possibly depending on the variety of definitions. The only observational estimate is $\Gamma = 0.16$ by

Wunsch (1999), which GFP11 suggested could be used to illustrate absolute diffusivity.

The hydrographic estimate of eddy diffusivity by GFP11 is generally consistent with independent estimations via Lagrangian tracer dispersion numerically advected with altimetric velocity (Marshall, 2006; Sallée et al., 2011), falling between 500 and 3,000 $m^2\ s^{\,1}$ within the ACC core and 2,000–3,500 $m^2\ s^{\,1}$ in the jet's equatorward flank. The resulting map of diffusivity can be explained by the suppression theory deduced from weakly nonlinear wave–mean flow interaction (Ferrari and Nikurashin, 2010), interpreted as that jet-induced advection reduces the duration of isopycnal mixing for the same water mass, leading to suppression of mixing length. The suppression of eddy stirring ceases in "leaky jets" associated with non-parallel shear flows and meanderings steered by the topography (GFP11; Sallée et al., 2011; Tamsitt et al., 2018). Klocker and Abernathey (2014) conducted numerical simulations to test the quantitativeness of the mixing length framework. They remarked that diffusivity could equivalently be estimated in a hypothetical unsuppressed mixing regime by either the eddy scale/tracer-based mixing length formulations if choosing =0.15 for the tracer-based mixing length, supporting the estimate by Wunsch (1999). These studies rationalize using the hydrographic variability method to quantify eddy diffusion.

3. Data and methods

3.1 Satellite altimetry for $\mathbf{U}_{\mathrm{eddy}}$

An observational estimate of characteristic eddy velocity U_{eddy} is obtained by altimetric velocity. The advent of synthetic aperture interferometric radar altimeter enabled to measure sea ice freeboard remotely, and its application to dynamic ocean topography has recently been developed (Armitage et al., 2018; Dotto et al., 2018; Mizobata et al., 2020). The present study adopts the monthly reconstructed 0.2° grid dynamic ocean topography from 2011 to 2020 by Mizobata et al. (2020) to derive the climatological geostrophic velocities (Fig. 2). This dataset has an advantage over the product by Armitage et al. (2018) as its empirical orthogonal function filtering can remove spurious stripe patterns.

U_{eddy} is calculated as the standard deviation of the altimetric flow speed (Fig. 2). Its reliability is underpinned by the mooring measurements at 113°E (Peña-Molino et al., 2016), which mark standard deviations of 0.04–0.06 m s^{-1} in zonal and meridional directions at the CDW layer (~500 dbar) over the continental slope of 500–4,000 m. The typical value of U_{eddy} is somewhat larger than the choice of FRE19 (0.017 m s^{-1}), as they adopted the temporal mean velocity from the same mooring data. In principle, U_{eddy} is the standard deviation of the cross-frontal velocity. However, in contrast to the ACC's mainstream, the flow field in the Antarctic margin is quiescent, and the mean flow directions are unclear (upper panel of Fig. 2). To bypass this problem, we simply define U_{eddy} as the root-mean-squared velocity, accounting for its good agreement with the direct flow measurement (Peña-Molino et al., 2016). The vertical variations of the eddy velocity are not considered since the dynamic topography does not

monotonically descend poleward in the subpolar zone (e.g., Yamazaki et al., 2020), and thus the gravest empirical mode technique performed by GFP11 is not applicable. Nevertheless, U_{eddy} adopted for CDW is deemed acceptable because the vertical attenuation caused by the geostrophic shear is considerably small by the quasi-barotropic flow structure (Meijers et al., 2010; Peña-Molino et al., 2016; Mizobata et al., 2020) and the CDW isopycnals shoaling to 200–400 dbar (Yamazaki et al., 2020).

3.2 CTD profiles for $\mathbf{L}_{\mathrm{mix}}$

The mixing length L_{mix} is calculated from the hydrographic variability using equation (3). Historical CTD profiles from the World Ocean Database (https://www.ncei.noaa.gov/), Argo Global Data Assembly Center (Argo, 2000), and Marine Mammals Exploring the Oceans Pole to Pole archive (https://www.meop.net/; Treasure et al., 2018) are compiled. Data for December–March and 1990 onwards are extracted and filtered to remove poorly flagged data and fragmented profiles. Thereafter, 1-dbar Akima interpolation is performed for the CTD profiles. Surface data averaged within the neutral densities (Jacket and McDougall, 1997) are then constructed (Fig. 3), corresponding to CDW (defined as 28.0–28.1 kg m^{-3}) and Antarctic Surface Water (ASW; defined as 27.9–28.0 kg m^{-3}). The bounding densities are selected based on the overturning streamfunction in the Indo-Pacific sector, whereas these definitions can change in the Atlantic sector (Lumpkin and Speer, 2007). Fig. 3 indicates that, in contrast to the meridional spiciness gradient of ASW being stronger than CDW, the thickness gradient of CDW is generally stronger than ASW. We compare results from the CDW and ASW layers to check the layer dependency of mixing length and the quantitativeness of estimation.

Previous studies have adopted potential temperature and spiciness as the isopycnal tracer φ (GFP11; FRE19). However, the diffusion of these tracers does not necessarily reproduce the PV diffusion in the real ocean, and it is unclear whether these tracers yield diffusivity k that is conformant to the eddy volume flux and the downgradient (i.e., Fickian) diffusion. Since the isopycnal thickness is a possible candidate for the PV-conservative tracer (e.g., Vallis, 2017), the present study compares the thickness-based L_{mix} estimates with the spiciness-based estimates. This comparison can demonstrate how estimated L_{mix} changes depending on the tracer variables and the validity of the previous estimates (GFP11; FRE19). Conservative Temperature, Absolute Salinity, and spiciness (at 0 dbar) are calculated using the Gibbs Sea Water Oceanographic Toolbox (http://www.teos-10.org/), and the layer thickness is derived from the pressure difference between the upper and lower isopycnal surfaces of each water mass (e.g., 28.0 and 28.1 kg m^{-3} for CDW).

Mapping isopycnal climatology onto 0.2° grids is performed with the radius basis function interpolation (Yamazaki et al., 2020), which can reproduce the best representative surface of noisy data nonparametrically in the least-squares sense. Grid data with no less than 10 points within a 75 km data radius are adopted, selecting grids with data from multiple years. Although the data coverage is

partially reduced at 30–60°E, a sufficient amount of data is found within the region of interest, particularly over the continental slope of 1,000–3,000 m. The correspondence observed among the 3,000 m isobath, CDW spiciness of 0.15 kg m^{-3}, and CDW thickness of 300 m (Fig. 3) guarantees the reliability of the interpolated field. After calculating deviations of surface data from the interpolated climatological field, root-mean-squared tracer variations $\sigma(\varphi)$ are derived in each grid from the deviation data within the 75 km radius. This procedure minimalizes artifacts in $\sigma(\varphi)$ due to the spatial variation of the tracer field within the data radius. Although the choice of the radius size is a trade-off between the data amount and the resolution, the data criterion (10 points within the 75 km radius) is determined by the characteristic scale of the continental slope topography and the degree to which the mixing length is not dependent on data amount. Our choice is comparable to the discussion by GFP11 that "about 5–10 stations per 100 km" is a reasonable baseline required for the L_{mix} calculation to capture the basic distribution patterns.

3.3 Validation of mixing efficiency

One of the largest uncertainties of diffusivity k lies within the mixing efficiency Γ. Based on equations (1) and (3), FRE19 indicated the along-slope variability of eddy condition in the East Antarctic margin via mapping standard deviation of isopycnal spiciness, while their formulation does not include Γ and spatially variable U_{eddy}, leaving some ambiguities for the absolute value of k. For a trial, we directly calculate Γ from the correlation coefficient between v and φ, using a 17-month mooring record (for 2010–2011) across the ASC in 113°E over the slope of 500–4,000 m (reported by Peña-Molino et al., 2016). Vertical/meridional linear gridding (by 50 dbar for 200–1,500 dbar and by 0.1° for 65.5–61.5°S) is performed for hourly meridional velocity and temperature profiles. Their correlation coefficient for 12 months (8,761 steps) is calculated for each grid, assuming that the temperature variation is aligned with the PV change and the temperature gradient is directed northward on average. Although the temperature is used for φ, the temperature variation is almost proportional to the spiciness variation within the layers of interest.

From the histogram of Γ, the estimated mean value is 0.12 for down-gradient cases and 0.10 for all cases (Fig. 4). If the mean eddy velocity steadily directs the downgradient of the mean temperature, the upgradient cases may be irrelevant to the climatological eddy condition. Wunsch (1999) derived $\Gamma = 0.16$ from a global inventory of mooring records, broadly consistent with our estimates but larger by 30–40%. We must admit that 12 months is too short to determine eddy statistics with certainty (additional low-pass filtering may effectively cut off uninterested short-term variations at the cost of underestimation), and the cross-slope section cannot represent the diverse flow regimes of the Southern Ocean. Nevertheless, we adopt the mixing efficiency $\Gamma = 0.16$ by Wunsch (1999) based on the general agreement with the local estimate. The validity of choice is further discussed in Section 5.1.

4. Result

4.1 Mixing length

The standard deviation and normed gradient of the isopycnal tracer φ of each water mass are shown in Figs. 5 and 6 for the spiciness and layer thickness, respectively. The large gradient of spiciness is found near the ACC's southern boundary (SB; defined as the southernmost extent of 1.5 °C isotherms) in ASW (27.9–28.0 kg m^{-3}), while in CDW (28.0–28.1 kg m^{-3}), the gradient is largest over the upper continental slope to the south of SB (Fig. 5; middle panels). The large standard deviation (top panels) broadly corresponds to its steep gradient. Relative to the spiciness, the thickness gradient is somewhat homogeneous, and the coherence between the standard deviation and gradient is less noticeable (Fig. 6). As in the spiciness, the steep thickness gradient of CDW is found in the proximity of the SB, indicating a poleward volume flux facilitated by the thickness diffusion.

The bottom panels in Figs. 5 and 6 are the mixing length L_{mix} derived from equation (3) for each tracer. The spatial distributions of the spiciness/thickness-based L_{mix} are analogous regarding their small values near the SB. These estimates are quantitatively consistent with the previous estimate by GFP11, where L_{mix} can exceed 150 km in the unsuppressed part of the ACC. Although the spiciness/thickness-based diagnostics are highly dependent on the choice of isopycnal layer, the two L_{mix} estimates for CDW and ASW exhibit the highest value of ~150 km in the ACC domain and its suppression towards the continental slope. These results suggest the robustness of the estimated L_{mix}. The spatial variation of L_{mix} is generally consistent with the jet-induced suppression theory (Ferrari and Nikurashin, 2010) as discussed in the following, while near-boundary turbulent suppression or "law of the wall" likely becomes more influential over the Antarctic margin than in the ACC domain, analogously to what GFP11 speculated.

The dependence of L_{mix} on the flow regime is shown in Fig. 7. The estimates of L_{mix} are averaged in bins of the mean flow speed and are individually shown for the ACC frontal zones following categorization by Orsi et al. (1995) (Figs. 1 and 2). Here, the frontal zones refer to the dynamic topography data of Mizobata et al. (2020); the subpolar zone (south of SACCF-S to the ASF): $<$ –1.85 m, the southern zone (from the SACCF-S to SACCF-N): –1.85 ~ –1.6 m, and the antarctic zone (from SACCF-N to PF): –1.6 ~ –1.0 m. Readers are advised to compare Fig. 7 with the result by GFP11 (their Fig. 10), which puts emphasis on the more energetic part of ACC to the north. In the Antarctic and southern zones, L_{mix} tends to decrease from 70–90 to 30–60 km as the flow speed increases to 0.5 m s^{-1}, indicating suppressed mixing due to wave–mean flow interaction. In the antarctic zone, L_{mix} partly increases with the mean flow exceeding 0.5 m s^{-1}, corresponding to leaky jets in the lee of topographic features (GFP11; Sallée et al., 2011; Tamsitt et al., 2018) such as the Kerguelen Plateau (~80°E) and the Southeast Indian Ridge (~150°E; see Fig. 2). On the other hand, L_{mix} is not so dependent on flow speed in the subpolar zone as in the ACC, ranging from 20 to 60 km. These results suggest that the jet-induced

mixing suppression previously documented in the northern part of the ACC is less effective poleward. We posit that the mixing suppression in the subpolar zone is likely associated with the near-boundary turbulent suppression by the continental slope topography and the flow regime more quiescent than the ACC domain. In Fig. 7, differences between CDW and ASW are unclear, accounting for the different data coverages of ASW and CDW (Fig. 3). Meanwhile, the thickness-based L_{mix} for ASW in the subpolar zone is exceptionally large for strong flows with relatively large standard errors, possibly due to the less distinct thickness gradient than spiciness in ASW (Figs. 5 and 6). Notably, while the choice of the isopycnal layer and tracer φ occasionally affects the outcome, the hydrographic variability method yields L_{mix} consistent with previous estimates (GFP11; FRE19).

To examine whether the tracer variance or inverse tracer gradient is more important in setting the L_{mix} variation, a histogram of L_{mix} is plotted on $\sigma(\varphi)$ $1/|\nabla\varphi|$ space (Fig. 8), in which the isolines of $L_{\mathrm{mix}} = 20$, 100 km are shown by white contours. The poleward suppression of L_{mix} is observed by comparing the positions of the largest population and center of mass among the frontal zones. In all presented layers and methods, modes and averages of L_{mix} are aligned with the $1/|\nabla\varphi|$ axis in the antarctic zone, and they migrate towards the $\sigma(\varphi)$ axis across the diagonal line as moving poleward. A key conclusion from this plot is that the inversed tracer gradient $1/|\nabla\varphi|$ becomes more influential poleward to the spatial variation of L_{mix} than $\sigma(\varphi)$ does (i.e., the variation of L_{mix} in the cross-isoline direction is hardly explained by $\sigma(\varphi)$ in the subpolar zone in contrast to the Antarctic and southern zones). This control might be because the poleward PV gradient becomes steeper (equivalently, the width of baroclinic zone becomes narrower) to the south, plausibly due to the continental slope topography. The topographic control of L_{mix} implicates a possibility of parameterizing the eddy diffusivity using prescribed topographic information in an ocean model, as recently explored by idealized numerical simulations (Stewart and Thompson, 2016). We anticipate that, in the subpolar zone, L_{mix} and k can be predicted by the topographic gradient, and this idea will be assessed in the next section.

4.2 Isopycnal diffusivity

Based on the conformance of the results in the ACC domain with those of previous studies, the diffusive parameters in the Antarctic margin are further investigated. The along-slope variation of the thickness-based mixing length for CDW is represented in Fig. 9 (middle panel), which is generally controlled by the thickness gradient rather than the thickness variability (top panel). Using the mixing length formulation of equation (1), the isopycnal diffusivity k is calculated by multiplying the mixing efficiency Γ, eddy velocity U_{eddy}, and mixing length L_{mix} (bottom panel). The isopycnal diffusivity for the two tracer variables is mapped in Fig. 10. Here, the climatological flow direction is represented by the overlain mean dynamic topography and contours that are characteristic of the subpolar circulation (1.97 and 1.85 m) highlighted in blue. Fig. 10

suggests that the isopycnal diffusivity k typically ranges from 100 to 500 $m^2\ s^{-1}$ in the subpolar zone for both tracer variables. Its variation within the subpolar zone is attributable to the spatial variation of L_{mix} (Figs. 5 and 6) rather than U_{eddy} (Fig. 2) as observed in Fig. 9. To scrutinize the spatial variability, regional maps of the thickness-based diffusivity along with the isopycnal CDW temperature are presented in Fig. 11. Diffusivity is typically higher where CDW intrudes onshore at 70°, 90°, 110°, and 120°E (Yamazaki et al., 2020) as seen in Fig. 9. The CDW intrusions generally corresponds to the smaller thickness gradient, resulting in the larger L_{mix} and higher k at the location (Fig. 11). The enhanced diffusivity is also observed at 140°E (Fig. 10), where the intervals between the ACC and ASC become narrow and clockwise subgyres are meridionally squeezed.

The spatial variation of k results from those of L_{mix} and U_{eddy}, and its functional dependency (i.e., control of k by L_{mix} and U_{eddy}) varies in space. A histogram of k in U_{eddy} L_{mix} coordinates is generated for each layer and method (Fig. 12), analogously to Fig. 8. In any of the frontal zones, neither L_{mix} nor U_{eddy} is a dominant controlling factor since both the population and center of mass are located close to the diagonal line. Nevertheless, we may state that k is more dependent on L_{mix} than U_{eddy} in the subpolar zone comparing to the southern or antarctic zones. The result supports the aforementioned idea that the spatial scale of tracer gradient can parametrize eddy diffusivity in the Antarctic margin. This idea is further tested by Fig. 13, in which k, L_{mix}, and inversed topographic gradient within the subpolar zone are regressed onto the inversed tracer gradient. The results show significant correlations (p-value < 0.01) of k and L_{mix} with $1/|\nabla\varphi|$ (0.62 and 0.78 for spiciness; 0.65 and 0.82 for thickness, respectively). In contrast, the correlation with the topographic gradient is insignificant for both tracers, implying that additional information is required to determine the climatological tracer gradient. Although the controlling factors for the tracer gradient field remain unknown, the derived correlations are still encouraging as it suggests a possibility that the eddy diffusion can be estimated by only providing the isopycnal tracer gradient.

The correlation of the thickness-based estimation with diffusivity is slightly more significant than the spiciness-based result. The higher correlation of thickness implies that the thickness gradient better represents the PV gradient, whereas the difference in the correlation coefficients can fall within the uncertainty. Provided that the ambient PV field is well approximated by the isopycnal layer thickness within the subpolar zone, where the flow condition is relatively quiescent and the relative vorticity tends to become small, the isopycnal thickness can be regarded as the PV-conservative variable. The mixing length framework principally requires that the diffusion of the tracer is Fickian, and this likely holds in case the tracer is PV-conservative (e.g., Vallis, 2017). In addition, the thickness diffusion is likely more representative of the eddy volume transport (eddy advection) than the spiciness diffusion. Predicated on these conditions, we estimate diffusive fluxes by applying the thickness-based diffusivity.

4.3 Eddy fluxes

Assuming that the isopycnal thickness diffuses downgradient in a GM-flux manner, we can estimate the diffusive volume flux of CDW (Fig. 14). Bolus transport ψ is calculated as

$$\psi \ = \ -k_H \nabla \mathrm{H} \qquad (5),$$

where H and k_H are the isopycnal layer thickness and thickness-based diffusivity, respectively. ψ is equivalent to the layer-integrated bolus velocity (in $m^2\ s^{-1}$), and its horizontal integration gives a unit of transport. The zonal eddy transport (middle panel) is typically eastward in the lee of topography and westward in the other area, reflecting the directions of the streamline and the thickness gradient steered by the topography. The eddy volume transport generally directs shoreward in the subpolar zone, as shown by the transport vector (top panel) and its meridional component (bottom panel). We can observe the poleward CDW transport continuously extending from the eastern flank of the Kerguelen Plateau, where isopycnal eddies are favorably generated, facilitating the CDW flux towards the Antarctic margin. Along-slope variation of the meridional eddy transport is not so pronounced as k (Fig. 10), and the most significant poleward CDW transport is obtained around 140°E. This result is related to the fact that the magnitude of eddy transport is $|\psi| = \ \Gamma U_{\mathrm{eddy}} \sigma(H)$ by equation (3) and is not proportional to the inversed thickness gradient (whether the CDW flux becomes uniquely proportional to U_{eddy} is unclear even in zonally-symmetric configuration due to possible variability of mixing efficiency; e.g., Stewart and Thompson, 2016). Partially northward eddy transport along the continental slope (e.g., around 70°E) likely reflects the multiple-cored ASC over the gentle continental slope, which has emerged in previous literature (Meijers et al., 2010; Stewart and Thompson, 2016).

The meridional component of ψ is zonally integrated to derive the cross-slope fluxes over the 1,000–3,000 m isobaths (Fig. 15). Strictly, this is not the cross-isobath transport, whereas the method does not lose its fidelity regarding the averaging depth range within which the direction of the slope gradient greatly varies. Standard errors associated with the cross-slope variation are shaded. The gross onshore CDW transport is 0.39/0.12 Sv ($= m^3\ s^{-1}$) in the eastern/western Indian sectors (divided by the Princess Elizabeth Trough ~90°E), respectively. Using the along-slope average of the sensible heat of CDW, these transports are translated to the onshore heat fluxes of 3.6/1.2 TW, where the heat flux change due to the along-slope temperature variation safely falls within the error range. The interbasin contrast in the thermal forcing, wherein a more significant amount of heat is transported onshore in the eastern sector than in the western sector, seems consistent with the coastal regimes, represented by warm Totten Ice Shelf and cold Amery Ice Shelf (Stokes et al., 2022).

Offshore transport of ASW (defined as 27.9–28.0 kg m^{-3}) to the west of 130°E is 0.15 Sv, locally compensating ~40 % of the onshore volume flux by CDW. In

contrast, ASW eastward of 130°E is transported to the pole, and its contribution to the onshore heat flux (~0.4 TW) might not be negligible. As discussed in Section 5.3, these estimates are quantitatively consistent with the coastal heat sink due to sea ice formation and glacial melting.

5. Discussion

5.1 Diffusivity estimation

The present study is fundamentally based on the assumption that the mixing length framework is valid to the extent of our interest. One of the necessary conditions for the formulation (see Section 2) is a scale separation between L_{mix} and the spatial variation of $\nabla\varphi$. We estimated the typical value of L_{mix} to be 20–60 km in the subpolar zone (Fig. 7). $\nabla\varphi$ likely varies in the cross-slope direction by a scale comparable to or larger than the slope width (~100 km for the 1,000–3,000 m interval), so it is possible to regard this condition as holding in the Antarctic margin. The other necessary condition for L_{mix} estimation is that tracer fluctuations must reflect local eddy stirring rather than tracer anomalies advected from upstream. This condition also holds in the Antarctic margin, given its weaker nonlinearity than the ACC's mainstream (Fig. 3). Another caveat for the method is that the estimates of tracer variance are obtained from anomalies relative to the climatological mean field spreading within a data radius (75 km in this study), whereas the formulation of the mixing length employs a temporal average over fluctuations at a spatially fixed point. Although this issue is inevitable when deriving diagnostics from in-situ data, an appropriate choice may be obtained by testing the result's sensitivity to the data radius (Section 3.2).

No significant difference is found between the thickness-based and spiciness-based L_{mix} (Figs. 5 and 6). To our knowledge, the present study is the first example to demonstrate that the two choices of tracer yield very similar L_{mix} estimates based on hydrographic variability. This result supports the validity of previous estimates in which isopycnal tracers physically independent of PV are used (GFP11; FRE19; Armi and Stommel, 1983). Meanwhile, a small but noticeable difference between the spiciness/thickness-based estimations is obtained; e.g., the large thickness-based (spiciness-based) k in 70°E (110°E) seems weak by the counterpart method (Fig. 10). The flow speed dependency of L_{mix} can also vary by choice of tracer (Fig. 7). These generally pertain to the regional difference in the tracer gradient, as the large diffusivities tend to result from the weak tracer gradient. The quiescent flow regime in the subpolar region indicates that the isopycnal thickness may be deemed more PV-conservative than in the ACC. Although the spiciness variation can also be used for the mixing length estimation, the PV-conservative nature of isopycnal thickness and the thickness-based L_{mix} rationalize the calculation of thickness-diffusive transport.

The estimated diffusivity of 100–500 $\mathrm{m^2\ s^{-1}}$ is significantly smaller than the along-slope estimation of $950 \pm 400\ \mathrm{m^2\ s^{-1}}$ by FRE19. However, their estimation was for the relative diffusivity in that they implicitly assumed the mixing

efficiency Γ to be unity (far exceeding its range; 0.01–0.4) and hence seems incompatible with our estimation. If $\Gamma = 0.16$ by Wunsch (1999), also supported by Klocker and Abernathey (2014), is consistently applied for their values, the isopycnal diffusivity of 90–220 m^2 s^{-1} is obtained, somewhat smaller k than our estimates. Further, our estimation is consistent with previous studies in the ACC's mainstream, typically ranging 500–2000 m^2 s^{-1} (Marshall et al., 2006) and 1500–3000 m^2 s^{-1} (Sallée et al., 2011) with a poleward decrease. Although the uncertainty of k is inaccessible and the mixing length estimated from the hydrographic variability does not necessarily reflect diffusion solely due to eddies by principle, the accordance with the estimations derived from the altimetric speed supports its plausibility.

One of the most uncertain parts is the spatial variability of mixing efficiency. Visbeck et al. (1997) argue that the eddy transfer coefficient, which determines the proportionality of diffusivity to the horizontal/vertical stratification and the width of the baroclinic zone, is a universal constant (equal to 0.015) regardless of the flow regime. Mixing efficiency is different from this coefficient by its formulation, but they are possibly associated with each other. The mooring data (Section 3.3) and the argument by Klocker and Abernathey (2014) generally support the local validity of $\Gamma = 0.16$ by Wunsch (1999). However, its global applicability is a future task and requires the utility of numerical models. The spatial variation of Γ can alter the correspondence between the enhanced diffusivity and the CDW intrusions (Fig. 11), while the along-slope analysis leastwise suggests that the mixing length becomes larger where CDW intrudes shoreward (Fig. 9). Furthermore, it is presumable that the effect of its spatial variation is negligible when considering a basin-wide transport as performed in Fig. 15.

5.2 Variability in the Antarctic margin

L_{mix} and k tend to be larger where the onshore CDW intrusion occurs (Figs. 9 and 11). The scale of this correspondence is observed in a somewhat larger scale than the data radius = 75 km, which provides the highest limit of the resolving scale. This result supports that the cross-slope eddy flux is fundamental for transporting CDW onto the shelves. Since the intrusion sites are strongly associated with the topography-controlled subgyres (Yamazaki et al., 2020), the structure of the subpolar gyre and bathymetric feature are expected to be essential for determining the eddy field. The locations of CDW intrusion in Fig. 9 and the major contribution of eddy fluxes are reproduced in an eddy-resolving simulation (Stewart et al., 2018). The isopycnal fields further indicate that the CDW thickness gradient tends to be gentle where the intrusion occurs (Figs. 9 and 11). This situation likely pertains to the tracer gradient control on L_{mix} and k (Figs. 8 and 12). In the ACC domain, however, k is more dependent on U_{eddy} and $\sigma(\varphi)$ than in the subpolar region (Figs. 8 and 12), and thus L_{mix} is more related to the flow speed via the jet-induced suppression mechanism (Fig. 7). These results highlight the transition of the Southern Ocean eddy regime towards the Antarctic margin.

The correspondence between the CDW intrusion and gentle thickness gradient further suggests that the baroclinic structure of the ASC behaves as a barrier to the onshore CDW intrusion, as hypothesized by modeling studies (Thompson et al., 2018). The theoretical prediction of jet-induced mixing suppression (Ferrari and Nikurashin 2010) might be consistent with the unintrusive situation associated with a steep thickness gradient associated with the ASC; however, we could not obtain L_{mix} dependency on flow speed (Fig. 7). Although this is perhaps because of the coarse resolution of the altimetric velocity data (1/4°) with respect to the scale of ASC, currents in the subpolar zone are weaker than the ACC (Fig. 2), and the ASC is not as distinguished as the ACC jets (Peña-Molino et al., 2016), implying that the jet-induced suppression is not necessarily the primary factor for the shoreward eddy diffusion.

The dynamic driver governing the isopycnal thickness field remains unknown, yet we can posit that topographic steering plays an indispensable role. To investigate meridional overturning circulation across the ASC jets in a zonally symmetric configuration, Stewart and Thompson (2016) demonstrated that L_{mix} scaled by slope width accurately predicts the simulated onshore flux of CDW ($\mathrm{R}^2 = 0.89$). In contrast, our estimated L_{mix} is significantly correlated with the thickness gradient but not with the topographic gradient (Fig. 13). This result might be due to the indispensable role of the surface layer and distribution of ASW in controlling the layer thickness.

5.3 Eddy flux and heat budgets

The shoreward eddy heat flux (Fig. 15) is quantitatively consistent with the previously reported coastal budgets; integrating within the eastern Indian sector (90–160°E), the annual cumulative sea ice production is 520 ± 75 km^3 (Tamura et al., 2016; accounting for Shackleton, Vincennes, Dalton, Dibble, and Mertz Polynyas), translated to heat loss of 4.2–5.6 TW. On the other hand, the integrated ice shelf basal melt rate is 198 ± 39 Gt yr^{-1} (Rignot et al., 2013; accounting for Mertz, Dibble, Holmes, Moscow Univ., Totten, Vincennes, Conger, Tracy, and Shackleton Ice Shelves), translated to 1.7–2.5 TW. Therefore, the diffusive CDW heat flux of 3.2–3.9 TW (within the 28.0–28.1 kg m^{-3} neutral density) compensates for nearly half of the sum of cryospheric heat sinks by sea ice formation and ice shelf melt, and thus is a major source of heat for the Antarctic coasts. Missing source of heat (~3 TW) and offshore heat advection is likely balanced by the annual cumulative solar heating (~5 TW within 100 km from the coastline of 90–160°E; Tamura et al., 2011) and the partial onshore intrusion of ASW (to the east of 130°E). The volume imbalance between CDW and ASW may imply the local exporting flux of Antarctic Bottom Water, while an effect of convergent flux due to the along-slope mean flow cannot be distinguished in our analysis.

Results by Stewart and Thompson (2016) indicate a possibility of underestimating the onshore heat flux derived from the mixing length formulation when estimation is solely based on the thickness-diffusive CDW flux, or "eddy advection," because the isopycnal "eddy stirring" can also contribute to the heat flux

without transporting water volume, especially near the shelf break. The coastal heat budget closure by the eddy volume flux pertains to the situation that the eddy stirring and tidal mixing are not dominant over the targeted slope (1000–3000 m). This is consistent with a realistic simulation (Stewart et al., 2018), in which most of the heat flux explained by eddy advection over the isobaths subsequently reaches the Antarctic coast beyond the shelf break. The poleward CDW transport by the cross-slope geostrophic current was measured seaward of the 3000 m isobath (Mizobata et al., 2020), and this might be generally confined to the lower continental slope, regarding the numerical model (Stewart et al., 2018) and the trajectories of profiling floats (Yamazaki et al., 2020).

6. Summary and outlook

To describe the CDW diffusion towards the Antarctic margin, the present study conducted an extensive analysis of hydrographic measurements and satellite altimetry data. The mixing length formulation served as the primary basis for analysis. The spiciness/thickness-based estimations yielded similar results, which validated the mixing length estimates previously made using hydrographic variability. The same analysis was applied for ASW, and its mixing length close to CDW was obtained. Over the ACC domain (antarctic and southern zones), concurrences with previous studies on the mixing suppression theory and its exception in the lee of the topography (leaky jets) were found. However, the mixing length dependency on the mean flow was not found in the subpolar zone, reflecting a quiescent flow regime in the Antarctic margin. Mixing length tends to be larger where the CDW intrusion occurs. This observation is attributable to the thickness control on the diffusivity, in which the gentle thickness gradient allows for the ease of isopycnal mixing. Volume transport was estimated in a GM-flux manner, and the thickness-diffusive onshore heat flux over the continental slope was quantitatively consistent with cryospheric heat sinks (i.e., sea ice formation and ice shelf basal melt). Closure of the coastal heat budget was nearly achieved among the CDW eddies over the 1,000–3,000 m isobaths (+3.2 3.9 TW), solar heating (+5 TW), sea ice formation (4.2 5.6 TW), and basal melt of ice shelves (1.7 2.5 TW) for 90–160°E. This result suggests that the isopycnal eddy advection is substantial for the cross-slope CDW intrusion.

As a concluding remark, we underscore that the isopycnal thickness field is essential for determining the eddy fluxes in the Antarctic margin. Our findings allow predicting the eddy diffusivity by solely providing the layer thickness. This idea might be valuable for simulating CDW transport in climate models, where subgrid effects of eddy fluxes need to be parameterized. The mesoscale process is crucial for the multidecadal variability of onshore CDW flux (e.g., Yamazaki et al., 2021), and thus its appropriate expression in climate models is fundamental for projecting the Antarctic glacial melt with accuracy and confidence.

Acknowledgments

We are grateful to the Argo Program and the MEOP project for significant deployment efforts in the Southern Ocean and successive QC processes. B. Peña-

Molino provided the I9S mooring records. This study was financially supported by JSPS KAKENHI (grant number 21H04918, 22J00870). The authors declare no competing interest.

Open Research

All hydrographic data are available to the public, as detailed in Section 3.2. Dataset including dynamic ocean topography data (Mizobata et al., 2020) and Python codes used for figure creation can be downloaded from https://doi.org/10.5281/zenodo.6463138.

References

Abernathey, R. P., Cerovecki, I., Holland, P. R., Newsom, E., Mazloff, M., & Talley, L. D. (2016). Water-mass transformation by sea ice in the upper branch of the Southern Ocean overturning. *Nature Geoscience*, *9*(8), 596–601. https://doi.org/10.1038/ngeo2749

Argo (2000). Argo float data and metadata from Global Data Assembly Centre (Argo GDAC). SEANOE. https://doi.org/10.17882/42182

Armi, L., & Stommel, H. (1983). Four Views of a Portion of the North Atlantic Subtropical Gyre. *Journal of Physical Oceanography*, *13*(5), 828–857. https://doi.org/10.1175/1520-0485(1983)013<0828:FVOAPO>2.0.CO;2

Bates, M., Tulloch, R., Marshall, J., & Ferrari, R. (2014). Rationalizing the spatial distribution of mesoscale eddy diffusivity in terms of mixing length theory. *Journal of Physical Oceanography*, *44*(6), 1523–1540. https://doi.org/10.1175/JPO-D-13-0130.1

Cessi, P. (2019). The global overturning circulation. *Annual Review of Marine Science*, *11*, 249–270. https://doi.org/10.1146/annurev-marine-010318-095241

Dotto, T. S., Naveira Garabato, A., Bacon, S., Tsamados, M., Holland, P. R., Hooley, J., Frajka-Williams, E., Ridout, A., & Meredith, M.P., 2018. (2018). Variability of the Ross Gyre, Southern Ocean: Drivers and responses revealed by satellite altimetry. *Geophysical Research Letters*, 45(12), 6195-6204. https://doi.org/10.1029/2018GL078607

Ferrari, R., & Nikurashin, M. (2010). Suppression of eddy diffusivity across jets in the Southern Ocean. *Journal of Physical Oceanography*, *40*(7), 1501–1519. https://doi.org/10.1175/2010JPO4278.1

Foppert, A., Rintoul, S. R., & England, M. H. (2019). Along-Slope Variability of Cross-Slope Eddy Transport in East Antarctica. *Geophysical Research Letters*, *46*(14), 8224–8233. https://doi.org/10.1029/2019GL082999

Gent, P. R., & Mcwilliams, J. C. (1990). Isopycnal Mixing in Ocean Circulation Models. *Journal of Physical Oceanography*. https://doi.org/10.1175/1520-0485(1990)020<0150:imiocm>2.0.co;2

Hirano, D., Mizobata, K., Sasaki, H., Murase, H., Tamura, T., & Aoki, S. (2021). Poleward eddy-induced warm water transport across a shelf break off Totten Ice Shelf, East Antarctica. *Communications Earth & Environment*, *2*(1). https://doi.org/10.1038/s43247-021-00217-4

Hogg, A. M. C., & Blundell, J. R. (2006). Interdecadal variability of the Southern Ocean. *Journal of Physical Oceanography*, *36*(8), 1626–1645. https://doi.org/10.1175/JPO2934.1

Holloway, G., & Kristmannsson, S. S. (1984). Stirring and transport of tracer fields by geostrophic turbulence. *Journal of Fluid Mechanics*, *141*, 27–50. https://doi.org/10.1017/S0022112084000720

Jackett, D. R., & Mcdougall, T. J. (1997). A neutral density variable for the world's oceans. *Journal of Physical Oceanography*, *27*(2), 237–263. https://doi.org/10.1175/1520-0485(1997)027<0237:ANDVFT>2.0.CO;2

Karsten, R. H., & Marshall, J. (2002). Constructing the residual circulation of the ACC from observations. *Journal of Physical Oceanography*, *32*(12), 3315–3327. https://doi.org/10.1175/1520-0485(2002)032<3315:CTRCOT>2.0.CO;2

Klocker, A., & Abernathey, R. (2014). Global patterns of mesoscale eddy properties and diffusivities. *Journal of Physical Oceanography*, *44*(3), 1030–1046. https://doi.org/10.1175/JPO-D-13-0159.1

Kunze, E., Firing, E., Hummon, J. M., Chereskin, T. K., & Thurnherr, A. M. (2006). Global abyssal mixing inferred from lowered ADCP shear and CTD strain profiles. *Journal of Physical Oceanography*, *36*(8), 1553–1576. https://doi.org/10.1175/JPO2926.1

Lumpkin, R., & Speer, K. (2007). Global ocean meridional overturning. *Journal of Physical Oceanography*, 37(10), 2550-2562. https://doi.org/10.1175/JPO3130.1

Marshall, J., & Radko, T. (2003). Residual-mean solutions for the Antarctic Circumpolar Current and its associated overturning circulation. *Journal of Physical Oceanography*, *33*(11), 2341–2354. https://doi.org/10.1175/1520-0485(2003)033<2341:RSFTAC>2.0.CO;2

Marshall, J., Shuckburgh, E., Jones, H., & Hill, C. (2006). Estimates and implications of surface eddy diffusivity in the Southern Ocean derived from tracer transport. *Journal of Physical Oceanography*, *36*(9), 1806–1821. https://doi.org/10.1175/JPO2949.1

Mckee, D. C., Martinson, D. G., & Schofield, O. (2019). Origin and attenuation of mesoscale structure in Circumpolar Deep Water intrusions to an Antarctic shelf. *Journal of Physical Oceanography*, *49*(5), 1293–1318. https://doi.org/10.1175/JPO-D-18-0133.1

Meijers, A. J. S., Klocker, A., Bindoff, N. L., Williams, G. D., & Marsland, S. J. (2010). The circulation and water masses of the Antarctic shelf and continental slope between 30 and 80°E. *Deep-Sea Research Part II: Topical Studies in*

Oceanography, *57*(9–10), 723–737. https://doi.org/10.1016/j.dsr2.2009.04.019

Mizobata, K., Shimada, K., Aoki, S., & Kitade, Y. (2020). The Cyclonic Eddy Train in the Indian Ocean Sector of the Southern Ocean as Revealed by Satellite Radar Altimeters and In Situ Measurements. *Journal of Geophysical Research: Oceans*, *125*(6). https://doi.org/10.1029/2019JC015994

Morrison, A. K., McC. Hogg, A., England, M. H., & Spence, P. (2020). Warm Circumpolar Deep Water transport toward Antarctica driven by local dense water export in canyons. *Science Advances*, *6*(18), 1–10. https://doi.org/10.1126/sciadv.aav2516

Naveira Garabato, A. C., Ferrari, R., & Polzin, K. L. (2011). Eddy stirring in the Southern Ocean. *Journal of Geophysical Research: Oceans*, *116*(9), 1–29. https://doi.org/10.1029/2010JC006818

Orsi, A. H., Whitworth, T., & Nowlin, W. D. (1995). On the meridional extent and fronts of the Antarctic Circumpolar Current. *Deep-Sea Research Part I*, *42*(5), 641–673. https://doi.org/10.1016/0967-0637(95)00021-W

Padman, L., Siegfried, M. R., & Fricker, H. A. (2018). Ocean tide influences on the Antarctic and Greenland ice sheets. Reviews of Geophysics, 56(1), 142-184.

Park, Y. H., & Gamberoni, L. (1995). Large-scale circulation and its variability in the south Indian Ocean from TOPEX/POSEIDON altimetry. *Journal of Geophysical Research*, *100*(C12), 24911. https://doi.org/10.1029/95jc01962

Pauthenet, E., Sallée, J. B., Schmidtko, S., & Nerini, D. (2021). Seasonal variation of the antarctic slope front occurrence and position estimated from an interpolated hydrographic climatology. *Journal of Physical Oceanography*, *51*(5), 1539–1557. https://doi.org/10.1175/JPO-D-20-0186.1

Peña-Molino, B., McCartney, M. S., & Rintoul, S. R. (2016). Direct observations of the Antarctic Slope Current transport at 113°E. *Journal of Geophysical Research: Oceans*, *121*(10), 7390–7407. https://doi.org/10.1002/2015JC011594

Rignot, E., Jacobs, S., Mouginot, J., & Scheuchl, B. (2013). Ice-shelf melting around Antarctica. *Science*, *341*(6143), 266–270. https://doi.org/10.1126/science.1235798

Sallée, J. B., Speer, K., & Rintoul, S. R. (2011). Mean-flow and topographic control on surface eddy-mixing in the Southern Ocean. *Journal of Marine Research*, *69*(4–6), 753–777. https://doi.org/10.1357/002224011799849408

Shimada, K., Aoki, S., & Ohshima, K. I. (2017). Creation of a gridded dataset for the southern ocean with a topographic constraint scheme. *Journal of Atmospheric and Oceanic Technology*, *34*(3), 511–532. https://doi.org/10.1175/JTECH-D-16-0075.1

Spence, P., Holmes, R. M., Hogg, A. M. C., Griffies, S. M., Stewart, K. D., & England, M. H. (2017). Localized rapid warming of West Antarctic subsurface waters by remote winds. *Nature Climate Change*, *7*(8), 595–603. https://doi.org/10.1038/NCLIMATE3335

Stewart, A. L., Klocker, A., & Menemenlis, D. (2018). Circum-Antarctic Shoreward Heat Transport Derived From an Eddy- and Tide-Resolving Simulation. *Geophysical Research Letters*, *45*(2), 834–845. https://doi.org/10.1002/2017GL075677

Stewart, A. L., & Thompson, A. F. (2013). Connecting antarctic cross-slope exchange with southern ocean overturning. *Journal of Physical Oceanography*, *43*(7), 1453–1471. https://doi.org/10.1175/JPO-D-12-0205.1

Stewart, A. L., & Thompson, A. F. (2016). Eddy generation and jet formation via dense water outflows across the Antarctic continental slope. *Journal of Physical Oceanography*, *46*(12), 3729–3750. https://doi.org/10.1175/JPO-D-16-0145.1

Stokes, C. R., Abram, N. J., Bentley, M. J., Edwards, T. L., England, M. H., Foppert, A., ... & Whitehouse, P. L. (2022). Response of the East Antarctic Ice Sheet to past and future climate change. Nature, 608(7922), 275-286.

Tamsitt, V., Drake, H. F., Morrison, A. K., Talley, L. D., Dufour, C. O., Gray, A. R., et al. (2017). Spiraling pathways of global deep waters to the surface of the Southern Ocean. *Nature Communications*, *8*(1), 172. https://doi.org/10.1038/s41467-017-00197-0

Tamura, T., Ohshima, K. I., Fraser, A. D., & Williams, G. D. (2016). Sea ice production variability in Antarctic coastal polynyas. *Journal of Geophysical Research: Oceans*, *121*(5), 2967–2979. https://doi.org/10.1002/2015JC011537

Tamura, T., Ohshima, K. I., Nihashi, S., & Hasumi, H. (2011). Estimation of surface heat/salt fluxes associated with sea ice growth/melt in the Southern Ocean. *Scientific Online Letters on the Atmosphere*, *7*(1), 17–20. https://doi.org/10.2151/sola.2011-005

Taylor, G. I. (1922). Diffusion by Continuous Movements. *Proceedings of the London Mathematical Society*, *s2-20*(1), 196–212. https://doi.org/10.1112/plms/s2-20.1.196

Thompson, A. F., Speer, K. G., & Schulze Chretien, L. M. (2020). Genesis of the Antarctic Slope Current in West Antarctica. *Geophysical Research Letters*, *47*(16). https://doi.org/10.1029/2020GL087802

Thompson, A. F., Stewart, A. L., Spence, P., & Heywood, K. J. (2018). The Antarctic Slope Current in a Changing Climate. *Reviews of Geophysics*, *56*(4), 741–770. https://doi.org/10.1029/2018RG000624

Treasure, A. M., Roquet, F., Ansorge, I. J., Bester, M., Boehme, L., Bornemann, H., et al. (2017). Marine Mammals Exploring the Oceans Pole to Pole. *Oceanography*, *30*(2), 132–138. https://doi.org/10.5670/oceanog.2017.234

Vallis, G. K. (2017). *Atmospheric and Oceanic Fluid Dynamics, Second Edition.* Cambridge: Cambridge University Press. https://doi.org/10.1017/9781107588417

van Wijk, E. M., Rintoul, S. R., Wallace, L. O., Ribeiro, N., & Herraiz-Borreguero, L. (2022). Vulnerability of Denman Glacier to ocean heat

flux revealed by profiling float observations. Geophysical Research Letters, e2022GL100460.

Visbeck, M., Marshall, J., Haine, T., & Spall, M. (1997). Specification of Eddy Transfer Coefficients in Coarse-Resolution Ocean Circulation Models*. *Journal of Physical Oceanography*, *27*(3), 381–402. https://doi.org/10.1175/1520-0485(1997)027<0381:SOETCI>2.0.CO;2

Wunsch, C. (1999). Where do ocean eddy heat fluxes matter? *Journal of Geophysical Research: Oceans*, *104*(C6), 13235–13249. https://doi.org/10.1029/1999jc900062

Yamazaki, K., Aoki, S., Katsumata, K., Hirano, D., & Nakayama, Y. (2021). Multidecadal poleward shift of the southern boundary of the Antarctic Circumpolar Current off East Antarctica. *Science Advances*, *7*(24), eabf8755. https://doi.org/10.1126/sciadv.abf8755

Yamazaki, K., Aoki, S., Shimada, K., Kobayashi, T., & Kitade, Y. (2020). Structure of the Subpolar Gyre in the Australian-Antarctic Basin Derived From Argo Floats. *Journal of Geophysical Research: Oceans*, *125*(8). https://doi.org/10.1029/2019JC015406

Figures and Tables

Figure 1. Circulation and topography in the East Antarctic margin. The 3,000 m isobath is highlighted in white. Polar Front (PF; green), Northern/southern branches of Southern ACC Front (SACCF-N/S; yellow/magenta), and subpolar gyres (blue) are derived from dynamic ocean topography (Section 3.1), and Southern Boundary (SB; red) and Antarctic Slope Front (ASF, by 0°C at 400 dbar; cyan) are reproduced from temperature field of a climatological dataset by Shimada et al. (2017). The SACCF-S corresponds to the southernmost eastward jet of ACC (~4,000 m isobath), whereas the SB is located along the center of subpolar recirculating gyres (4,000–3,000 m) about zero lines of zonal velocity.

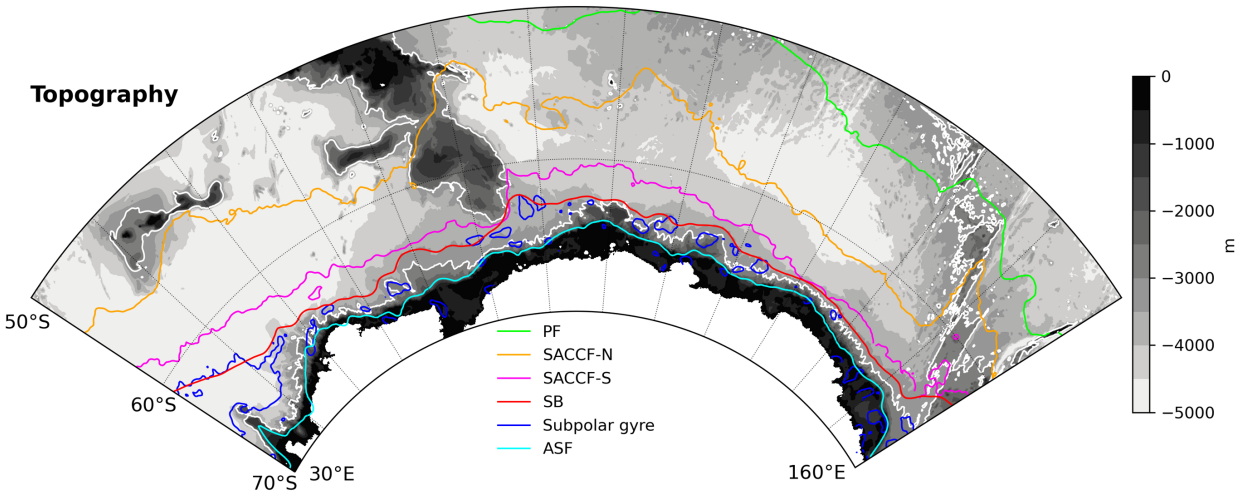

Figure 2. Altimetric flow speed averaged for 2011–2020. The upper panel is the temporal-mean geostrophic velocity, and the lower panel is the eddy velocity as root-mean-squared speed. Frontal positions are drawn as in Fig. 1.

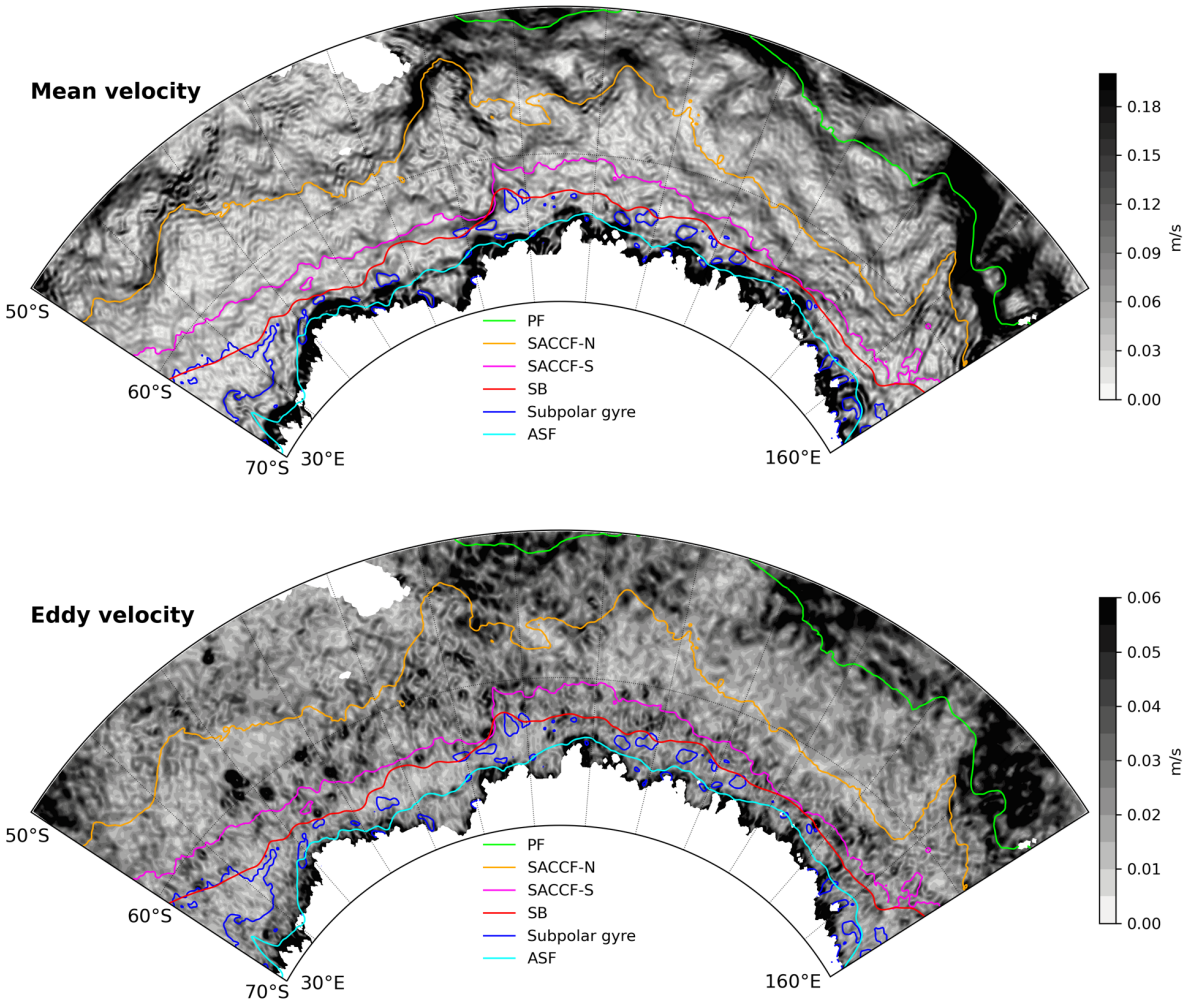

Figure 3. Distribution of hydrographic data and isopycnal watermass properties of ASW and CDW. Data density per 75 km data radius (top), Conservative Temperature (middle), and isopycnal pressure (bottom) are presented for ASW (left) and CDW (right). Areas with less than 10 data points within the 75 km radius are masked in gray. White contours in middle/bottom panels denote isopycnal spiciness/thickness (by 0.05 kg m^{-3}/100 m intervals), respectively, and the thick contour is –0.15 kg m^{-3}/300 m for each panel. SB (red) and isobaths with 1,000 m intervals (black) are also shown.

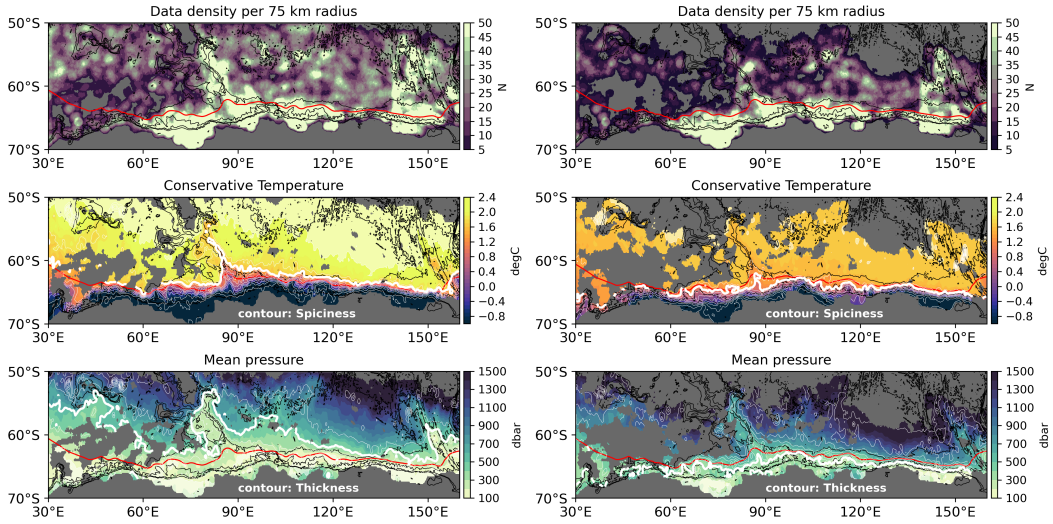

Figure 4. Histogram of mixing efficiency (or correlation coefficient between meridional velocity and temperature) from the cross-slope mooring section in 113°E. "Down-gradient" denotes the correlation by southward velocity (i.e., opposite to the temperature gradient), and "up-gradient" means the correlation by northward velocity. Since the downgradient flux must direct southward (shoreward), "up-gradient" possibly reflects transient events irrelevant to the climatological eddy condition. Hence, in addition to the whole mean (black line) and the previous estimate (dashed line; 0.16), the mean value only for the "down-gradient" is also presented (gray line).

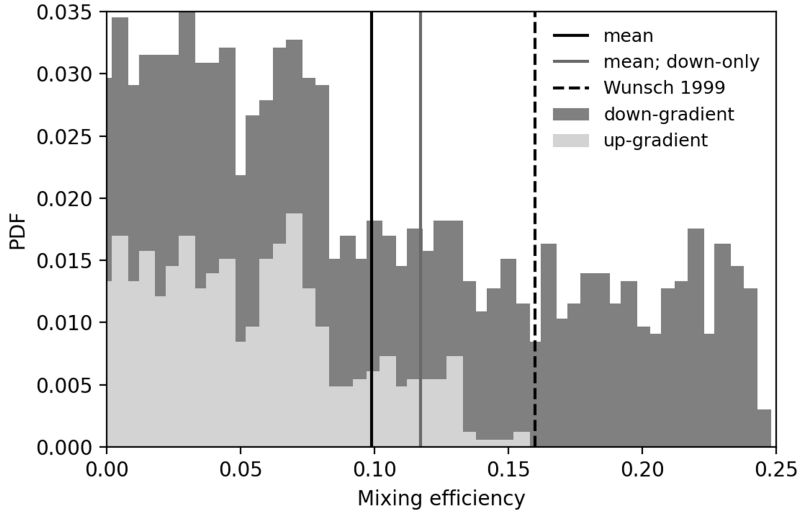

Figure 5. Mixing length calculation using isopycnal spiciness. Spiciness variability (top), normed spiciness gradient (middle), and mixing length (bottom) are presented for ASW (left) and CDW (right). White contours in top/middle panels denote isopycnal spiciness as of Fig. 3.

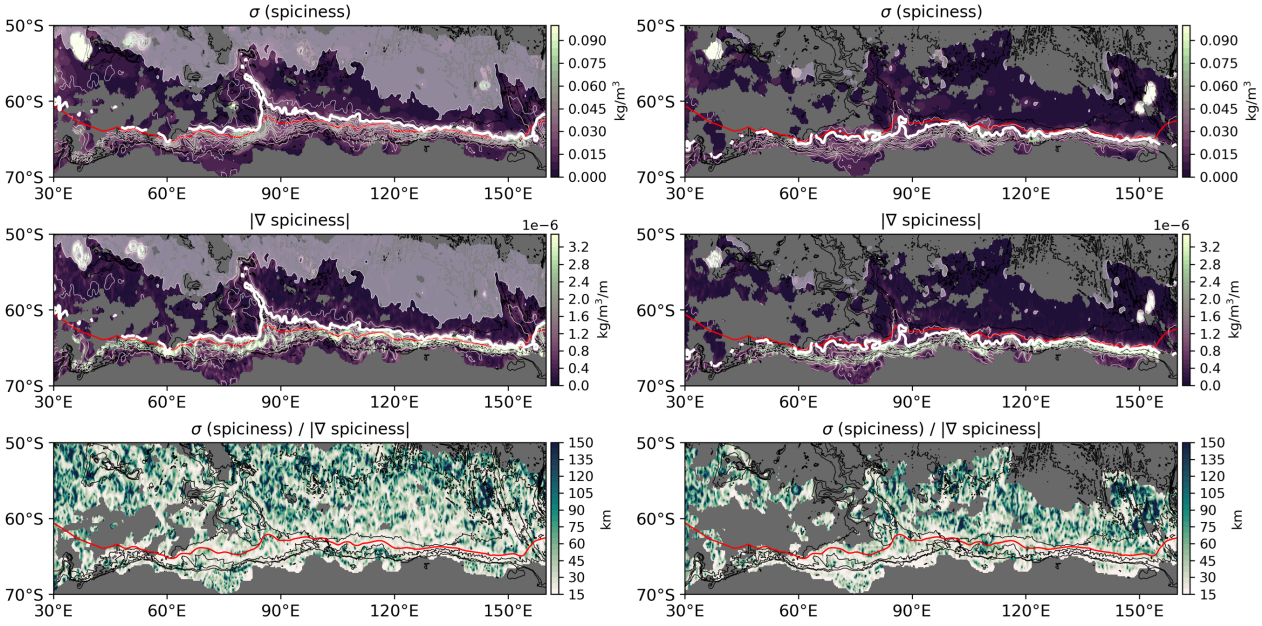

Figure 6. Mixing length calculation using isopycnal thickness. Thickness variability (top), normed thickness gradient (middle), and mixing length (bottom) are presented for ASW (left) and CDW (right). White contours in top/middle

panels denote isopycnal thickness as of Fig. 3.

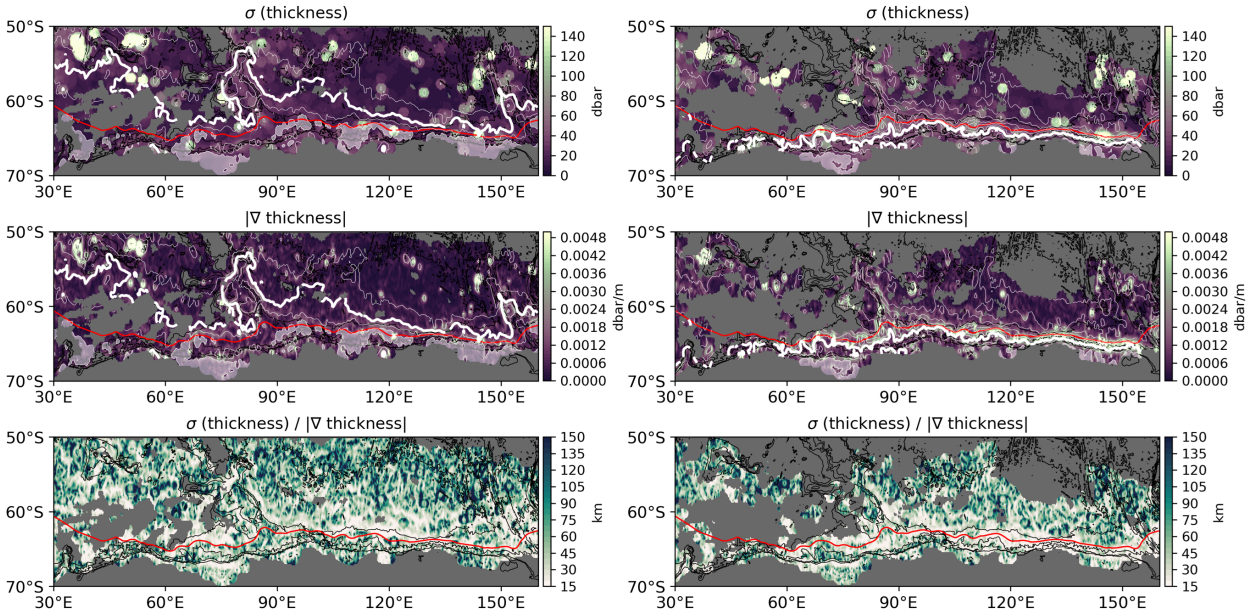

Figure 7. Mixing length dependency on the mean flow. Upper and lower panels are based on spiciness and thickness, and left/right panels are for ASW/CDW, respectively. The results are separately shown for the three frontal zones: subpolar (south of SACCF-S), southern (from SACCF-S to SACCF-N), and antarctic (from SACCF-N to PF) zones. Standard errors due to the spatial variation are shaded.

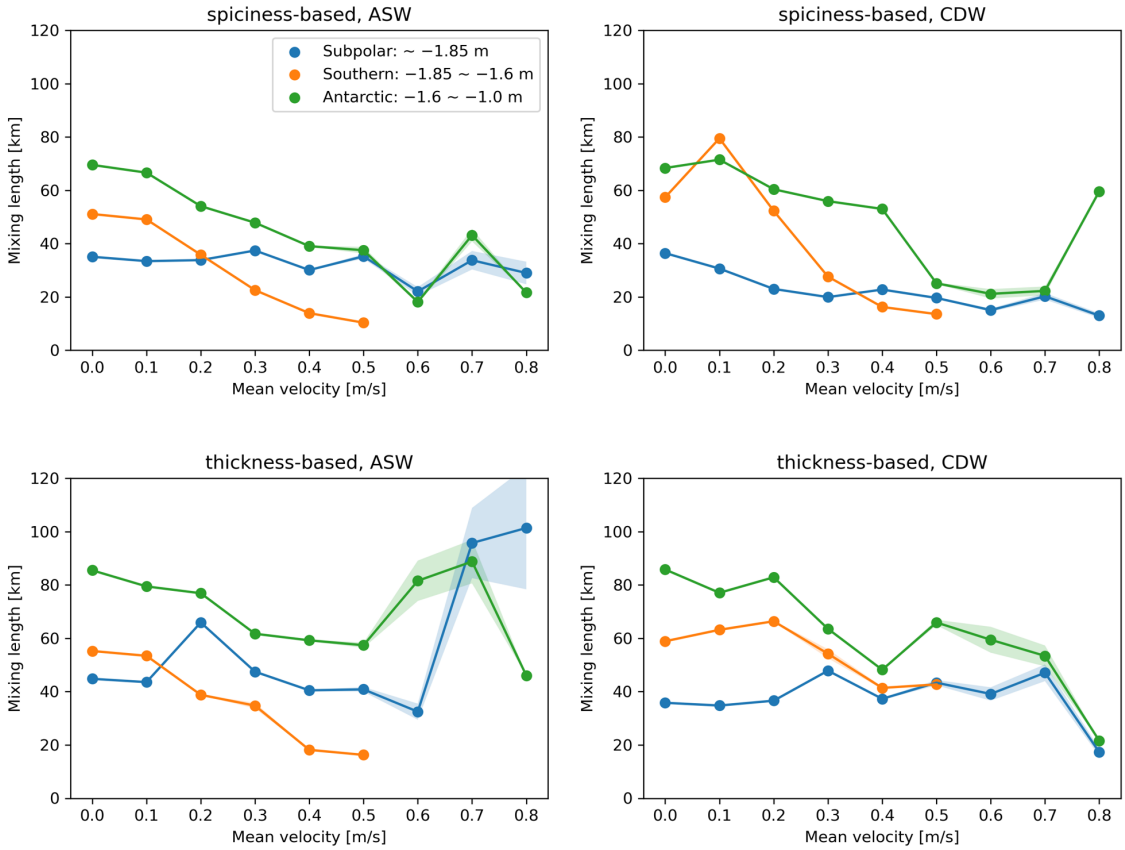

Figure 8. Two-dimensional histogram of mixing length as a function of tracer variability (horizontal) and inversed tracer gradient (vertical), indicating relative dependency of mixing length on the two variables. Rows correspond to the methods (spiciness and thickness) and layers (ASW and CDW), whereas columns correspond to the three frontal zones. Color shade is normalized to unity, and yellower indicates a larger data population. The axes are also normalized to illustrate their functional dependency. White cross denotes the averaged value of tracer variability and inversed tracer gradient, and white contours are the mixing length of 20 and 100 km. The diagonal dotted line indicates where controls by the two variables become comparable.

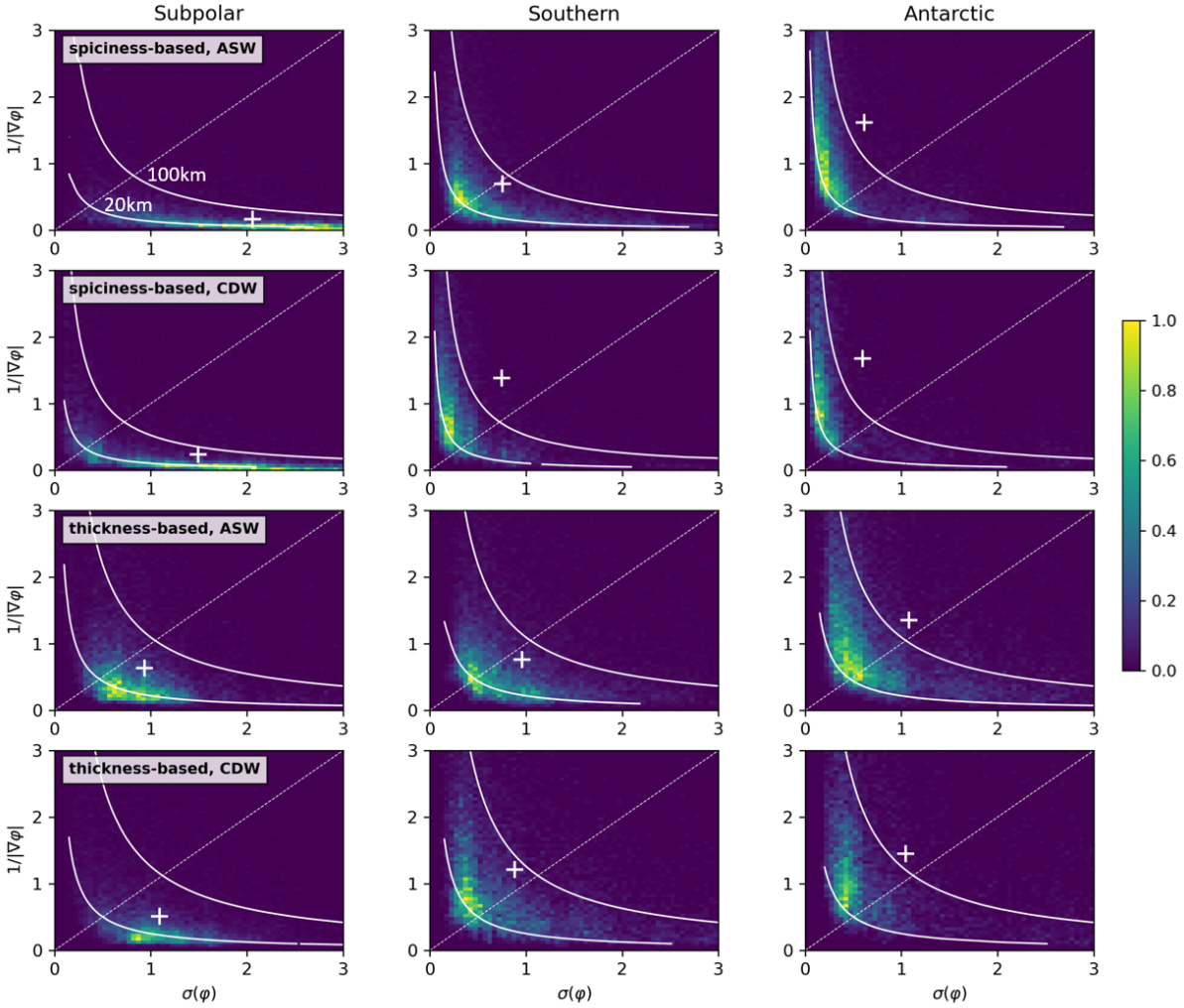

Figure 9. Along-slope variability of the diagnostics averaged within 1° bin in longitude over the 1,000–3,000 m isobaths. (top) Inversed gradient and standard deviation of the CDW thickness. (middle) thickness-based diffusivity and eddy velocity. (bottom) Isopycnal diffusivity for CDW. Red shades are the locations of CDW intrusion described in Yamazaki et al. (2020), where "Wx" is warm signals in the Australian-Antarctic Basin, "PB" is for the Prydz Bay, and "LHB" is for the Lützow-Holm Bay.

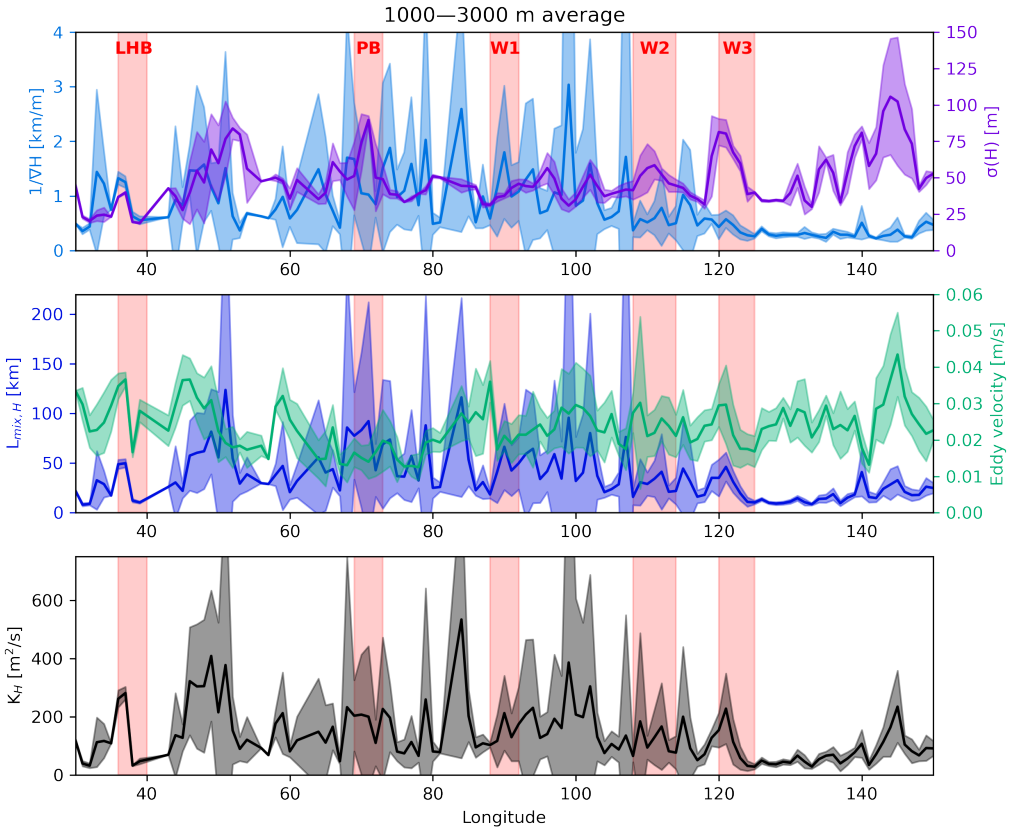

Figure 10. Spatial distribution of isopycnal diffusivity for CDW. Upper and lower panels are based on spiciness and thickness, respectively. In addition to SB (red) and isobaths, dynamic topography is overlaid by 2 cm intervals (white contours). Characteristic contours of dynamic topography are highlighted in blue (thick: subpolar gyre as –1.97 m, thin: SACCF-S as –1.85 m).

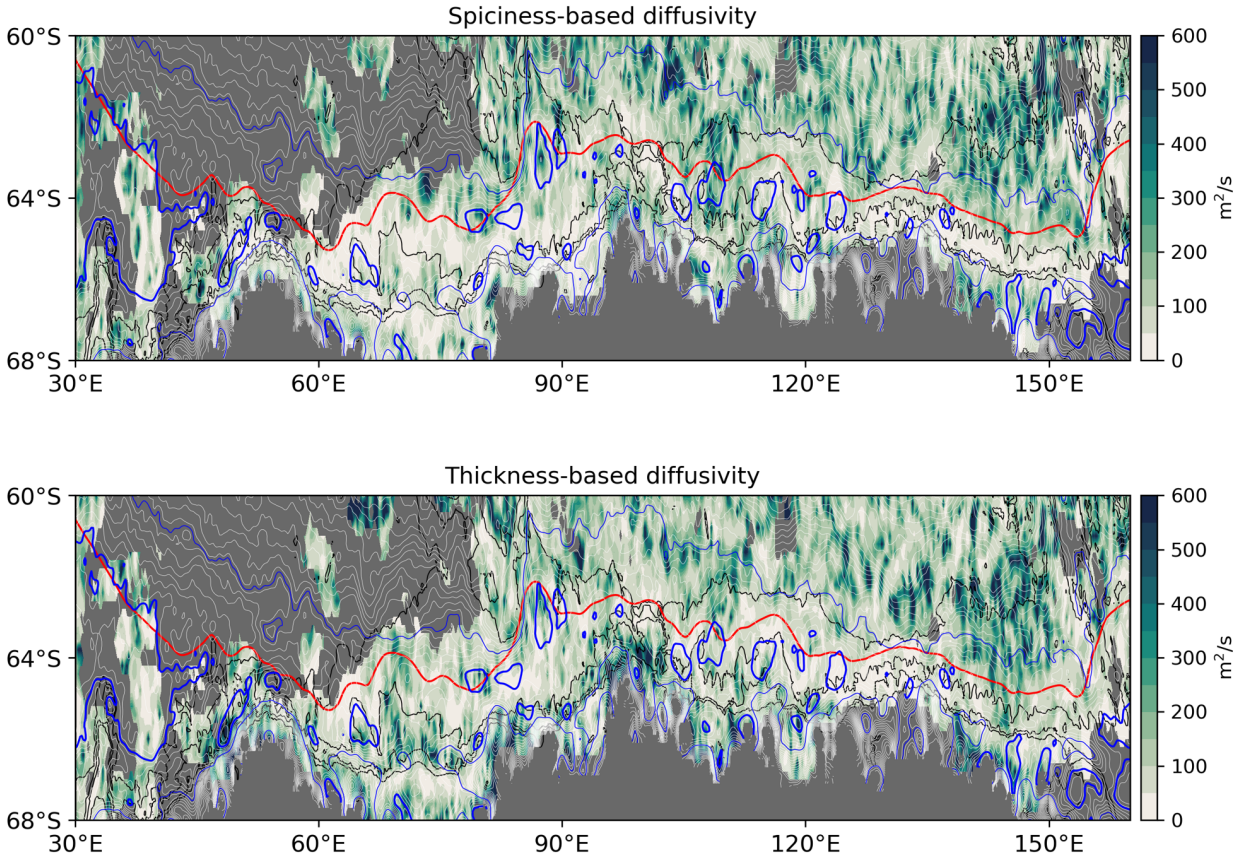

Figure 11. Eddy diffusion and CDW intrusion focusing on three key regions (Prydz Bay, Princess Elizabeth Trough, and off Wilkes Land). (top) Thickness-based diffusivity for CDW (Same as the lower panel of Fig. 10). (middle) The inversed thickness gradient. (bottom) The isopycnal temperature (same as Fig. 3). Vectors annotate where the CDW intrusion corresponds to the enhanced diffusivity.

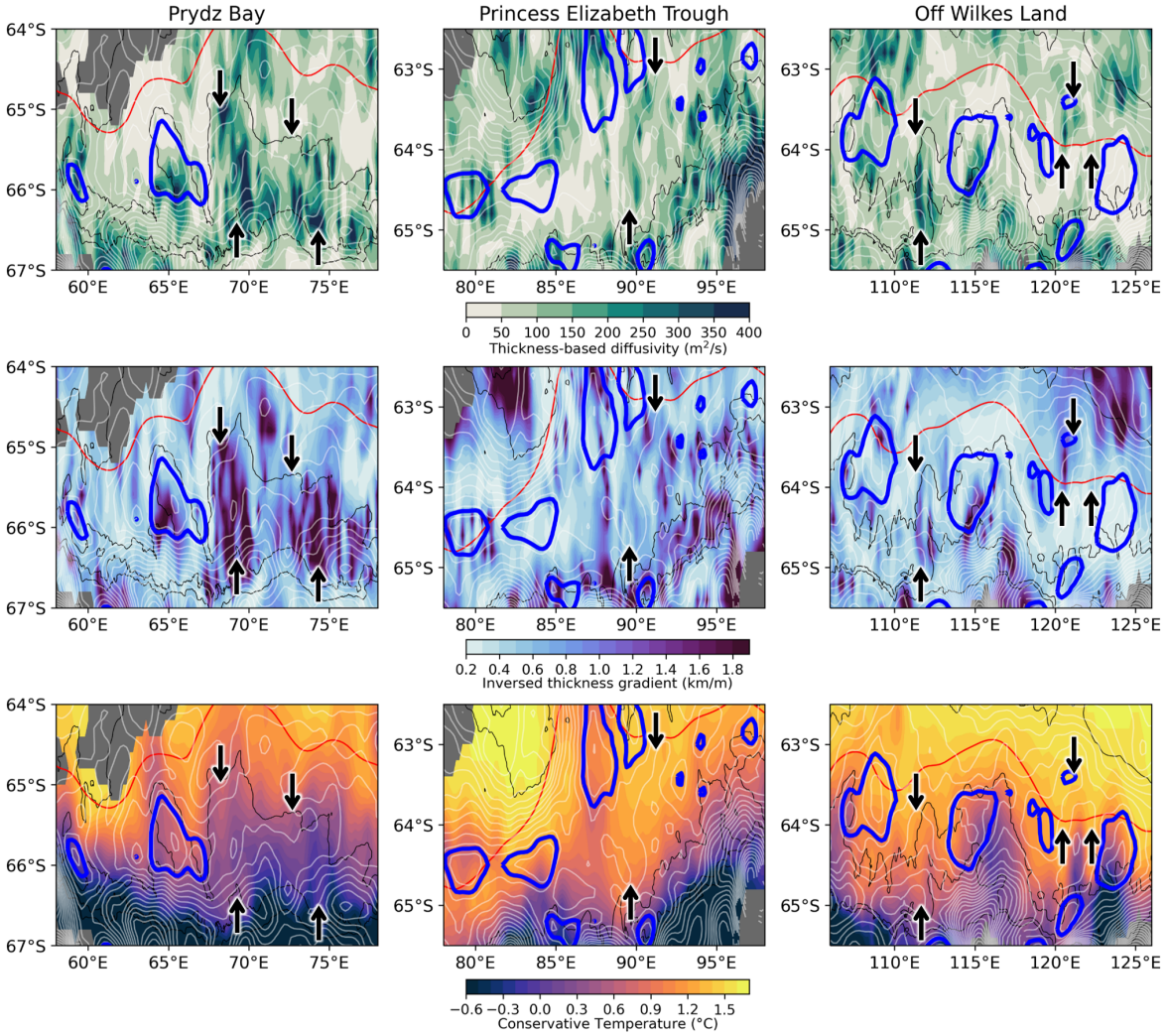

Figure 12. Histogram of isopycnal diffusivity on phase diagram as a function of eddy velocity (horizontal) and mixing length (vertical), analogously to Fig. 8. White contours denote the isopleths of 100 and 500 m^2 s^{-1}.

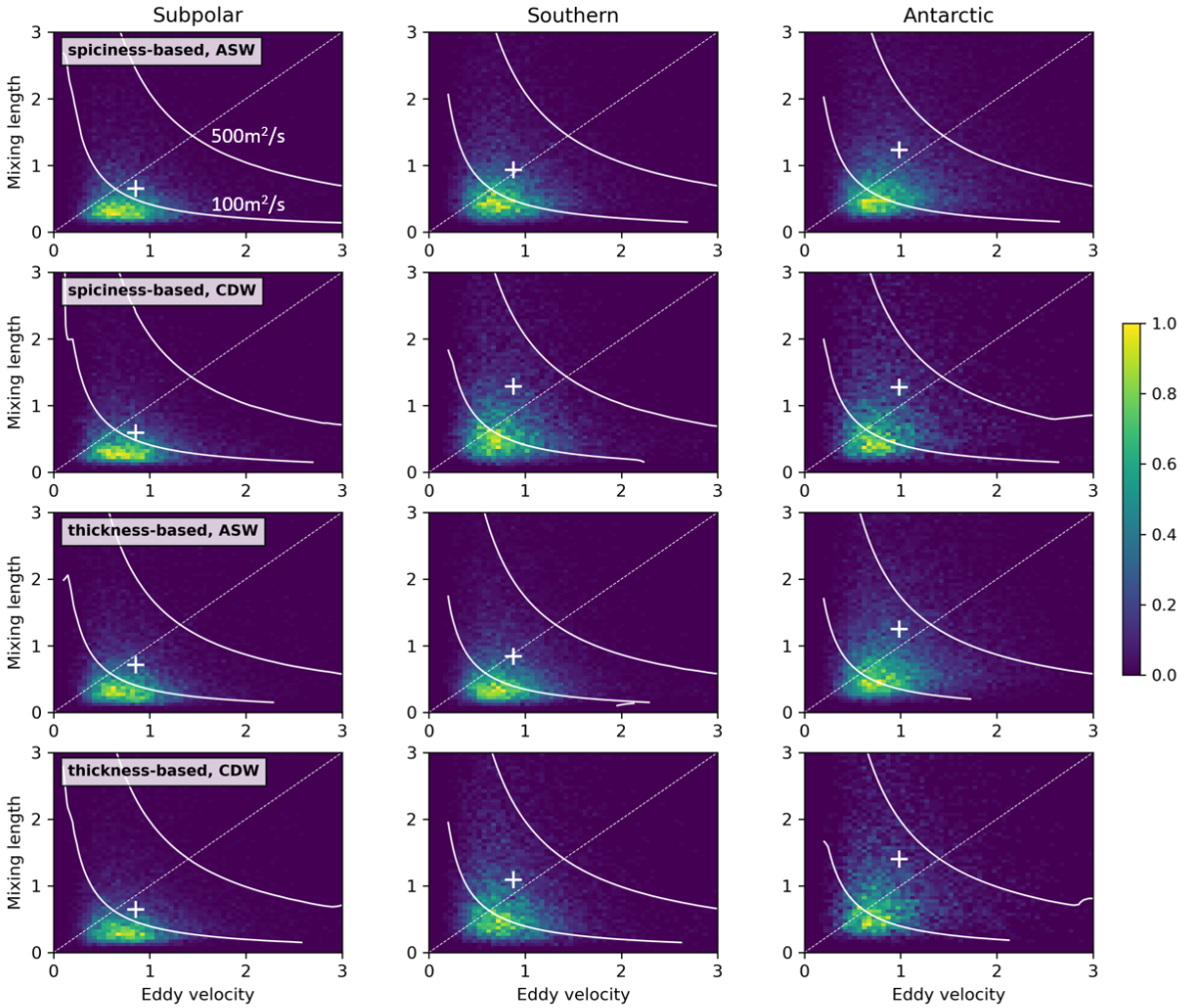

Figure 13. Tracer gradient control of CDW diffusion. Isopycnal diffusivity (top), mixing length (middle), and topographic gradient (bottom) over the 1,000–3,000 m isobath are regressed onto the inversed tracer gradient as spiciness (left) and thickness (right). The background color is the normalized histogram. Horizontal and vertical axes are normalized by the averages.

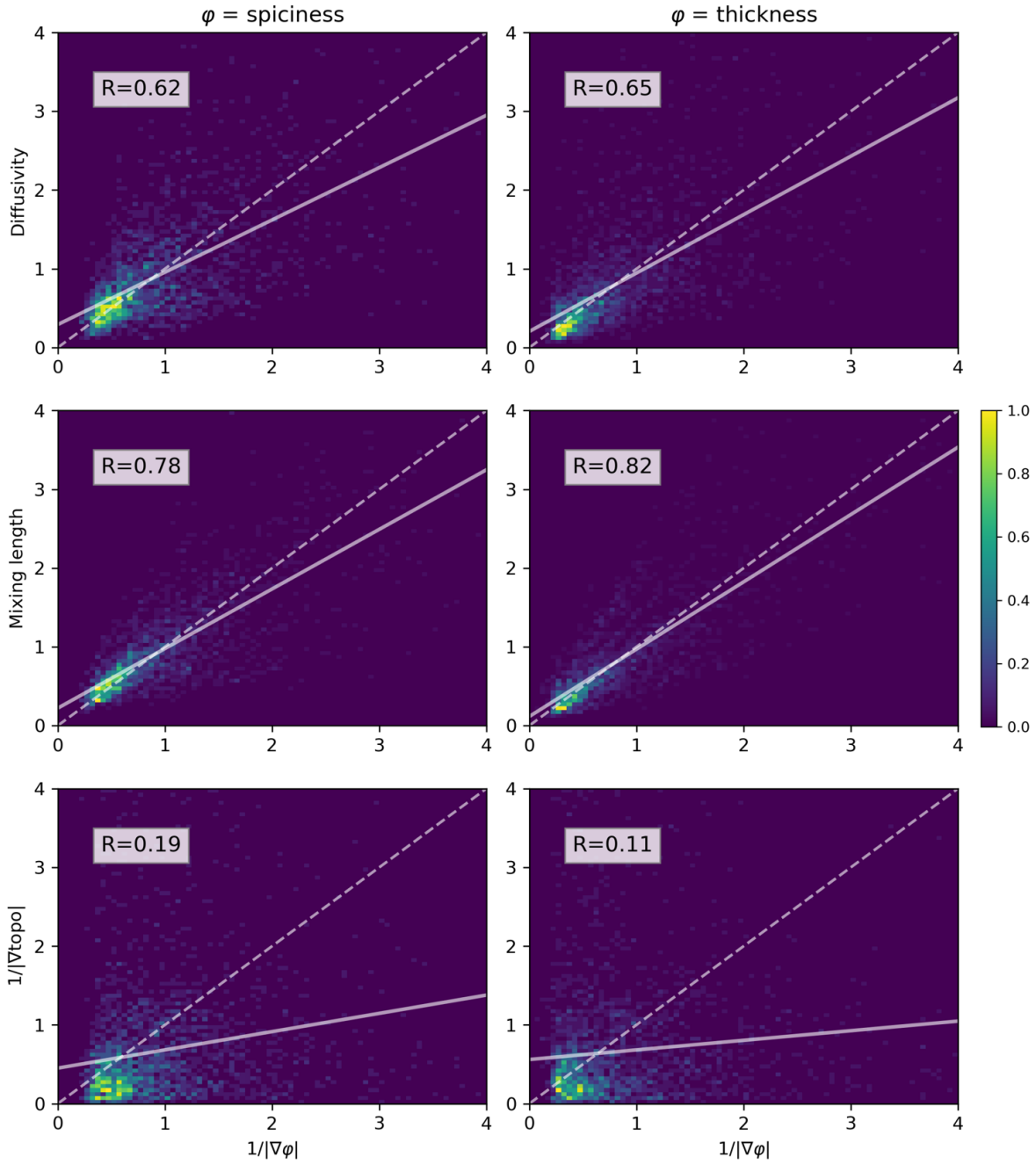

Figure 14. Spatial distribution of eddy CDW fluxes. The top, middle, and bottom panels are transport vectors, zonal and meridional transport, respectively. SB, isobaths, and dynamic topography are denoted as in Fig. 10. For

illustrative purposes, colormap for the meridional transport is flipped.

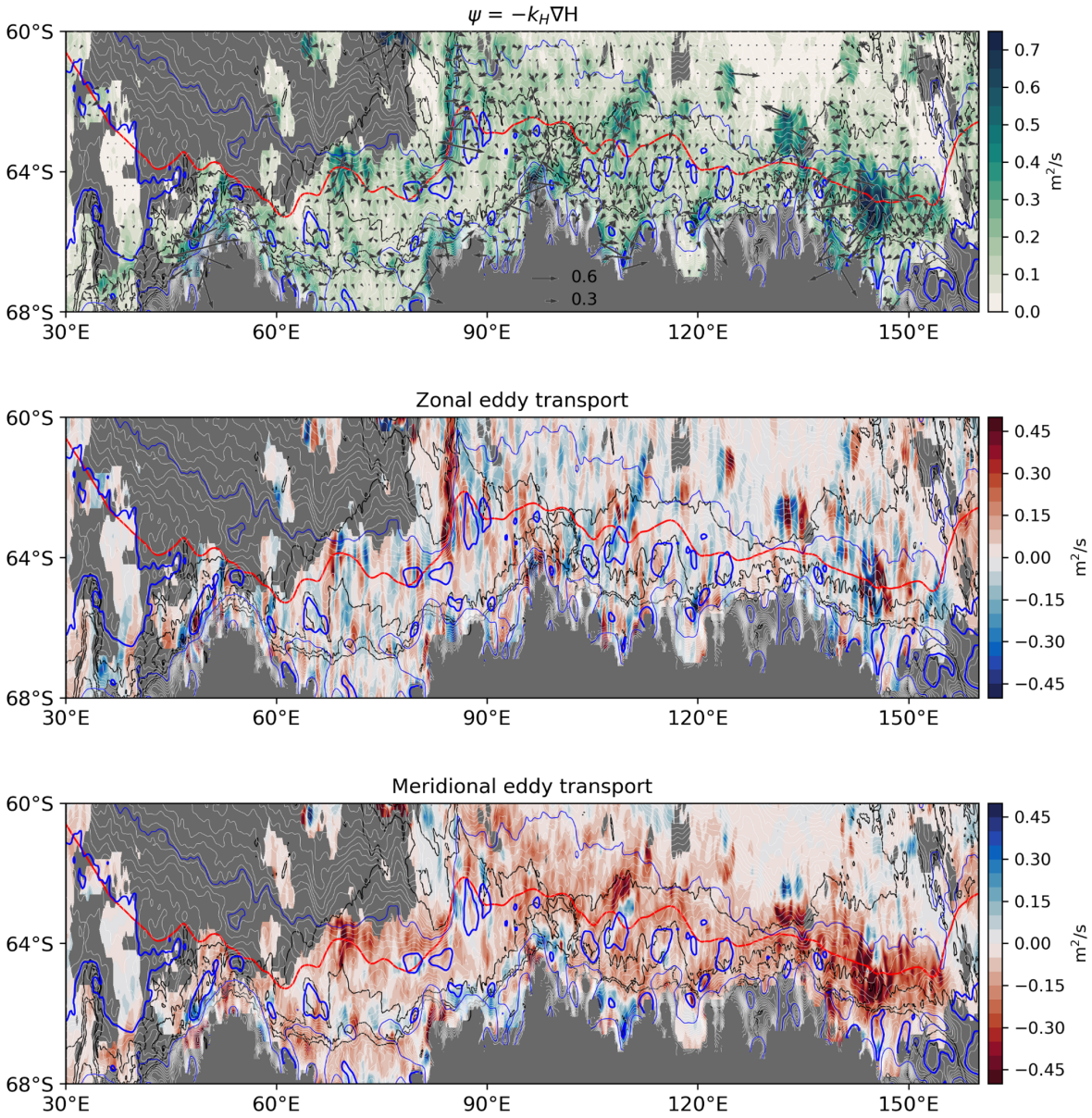

Figure 15. Cross-slope volume/heat transport. Meridional eddy transports for ASW and CDW (averaged in 1° bin over the 1,000–3,000 m isobaths) are zonally integrated. Standard errors due to the cross-slope variation are shown by shade. Volume transport can precisely be translated to heat flux using the mean temperature of CDW and ASW as indicated by ticks to the left. The 90°E meridian

for CDW corresponds to the interbasin boundary between eastern/western Indian sectors, while 130°E is the transitional longitude for the ASW transport direction.